Coastal Engineering 180 (2023) 104256

Contents lists available at ScienceDirect

Coastal Engineering

journal homepage: www.elsevier.com/locate/coastaleng

Towards a unified drag coefficient formula for quantifying wave energy reduction by salt marshes

Ling Zhu [a], Qin Chen [a,b,*], Yan Ding [c], Navid Jafari [d], Hongqing Wang [e], Bradley D. Johnson [c]

[a] Civil and Environmental Engineering, Northeastern University, Boston, MA 02115, USA
[b] Marine and Environmental Sciences, Northeastern University, Boston, MA 02115, USA
[c] U.S. Army Engineer Research and Development Center, Coastal and Hydraulics Laboratory, Vicksburg, MS 39180, USA
[d] Department of Civil and Environmental Engineering, Louisiana State University, Baton Rouge, LA 70803, USA
[e] U.S. Geological Survey, Wetland and Aquatic Research Center, Baton Rouge, LA 70803, USA

ARTICLE INFO

Keywords:
Wave attenuation
Flexible vegetation
Unified drag coefficient
Effective plant height

ABSTRACT

Coastal regions are susceptible to increasing flood risks amid climate change. Coastal wetlands play an important role in mitigating coastal hazards. Vegetation exerts a drag force to the flow and dampens storm surges and wind waves. The prediction of wave attenuation by vegetation typically relies on a pre-determined drag coefficient C_D. Existing C_D formulas are subject to vegetation biomechanical properties, especially the flexibility. Accounting for vegetation flexibility through the effective plant height (EPH), we propose and validate a species-independent relationship between C_D and the Reynolds number Re based on three independent datasets that cover a wide range of hydrodynamic conditions and vegetation traits. The proposed $C_D - Re$ relationship, used together with EPH, allows for predicting wave attenuation in salt marshes with high accuracy. Furthermore, a total of 308,000 numerical experiments with diverse wave conditions are conducted using the proposed $C_D - Re$ relationship and EPH to quantify the wave attenuation capacity of two typical salt mash species: *Elymus athericus* (highly flexible) and *Spartina alterniflora* (relatively rigid). It is found that wave attenuation is controlled by wave height to water depth ratio and EPH to water depth ratio. When swaying in large waves in shallow to intermediate water depth, a 50-m-long *Elymus athericus* field may lose up to 30% capacity for wave attenuation. As wave height increases, highly flexible vegetation causes reduced wave attenuation, whereas relatively rigid vegetation induces increased wave attenuation. The leaf contribution to wave attenuation is highly dependent on the leaf rigidity. It is recommended that leaf properties, especially its Young's modulus be collected in future field experiments.

1. Introduction

Climate change and sea level rise impose monumental challenges to urban coastal communities for developing resilient social and civil infrastructure. Coastal protection has historically relied on hard infrastructure (Stark and Jafari, 2015), such as levees, floodwalls, and surge barriers, but more attention has been drawn to natural and nature-based features (NNBFs) since Hurricane Katrina struck New Orleans in 2005 and Hurricane Sandy flooded New York City in 2012. NNBFs include marshes, mangroves, dunes, oyster reefs, among others, and they act as a natural buffer against wind, storm surges, and wind waves (Hu et al., 2015; Leonardi et al., 2016; Narayan et al., 2017; Jongman, 2018; Zhu and Chen, 2019b; Hochard et al., 2019; del Valle et al., 2020; Sun and Carson, 2020). Hard infrastructure supplemented with coastal wetlands has proved to be more sustainable and resilient in extreme events (Duarte et al., 2013; Nardin and Edmonds, 2014; Fagherazzi, 2014; Ganju et al., 2017; Editorial, 2021; Sheng et al., 2021) and reduce the likelihood and impact of overtopping and breaching of hard defenses (Zhu et al., 2020a). Quantifying the capacity of coastal wetlands, especially broadly distributed salt marshes, for wave attenuation is becoming pivotal for implementing NNBFs because it provides confidence in establishing a quantitative level of coastal flood protection (Schoutens et al., 2019).

The vegetation-induced drag (f_v) and energy dissipation rate (ϵ_v) are theoretically expressed as below (e.g., Dalrymple et al., 1984; Mendez and Losada, 2004):

$$f_v = \frac{1}{2}\rho C_D b_v N_v u_r |u_r| \quad \text{and} \quad \epsilon_v = \int_{-h}^{\min(-h+h_v^*,\eta)} f_v u_{\text{wave}} dz \tag{1}$$

in which ρ is the water density, b_v is the frontal width or diameter, N_v is the population density, h_v^* is the height of water column occupied

* Corresponding author.
E-mail address: q.chen@northeastern.edu (Q. Chen).

https://doi.org/10.1016/j.coastaleng.2022.104256
Received 24 January 2022; Received in revised form 7 November 2022; Accepted 20 November 2022
Available online 27 November 2022

by vegetation, h is the water depth, η is the surface elevation, C_D is the drag coefficient and u_r is the relative velocity between vegetation motions (u_{veg}) and surrounding water particle movements (u_{wave}), defined as $u_r = u_{\mathrm{wave}} - u_{\mathrm{veg}}$. The drag coefficient C_D is a key calibration parameter. Here, we list three major approaches to determine C_D:

1. measuring or modeling u_{veg}, computing u_r in Eq. (1) and back-calculating C_D from the wave height reduction (e.g., Maza et al., 2013; Zhu and Chen, 2015; Zhu et al., 2020b; van Veelen et al., 2020). Empirical C_D formulas that best-fit the calibrated C_D through this approach (e.g., Maza et al., 2013; Mattis et al., 2019; van Veelen et al., 2020) are theoretically species-independent. However, van Veelen et al. (2020)'s C_D formula, determined with regular waves, has not been tested against random waves. The best-fit C_D formula in Maza et al. (2013) did not show a high correlation coefficient.
2. simplifying $u_r = u_{\mathrm{wave}}$ in Eq. (1) and back-calculating C_D directly from the measured (e.g., Hu et al., 2014) or numerically simulated (e.g., Chakrabarti et al., 2016) vegetal drag.
3. simplifying $u_r = u_{\mathrm{wave}}$ in Eq. (1) and back-calculating C_D from the wave height reduction modeled by a theoretical energy dissipation model (e.g., Dalrymple et al., 1984; Mendez and Losada, 2004; Chen and Zhao, 2012; Losada et al., 2016). This approach is widely adopted in field and laboratory studies (e.g., Augustin et al., 2009; Wu et al., 2011; Paul and Amos, 2011; Jadhav et al., 2013; Anderson and Smith, 2014; Möller et al., 2014; Garzon et al., 2019). Most of the existing empirical C_D formulas were determined through this approach. However, the calibrated C_D integrates vegetation flexibility because of the omittance of u_{veg}. Thus, these empirical C_D formulas are species-specific and lack generality (Houser et al., 2015).

In a separate effort from using the theoretical expressions in Eq. (1), a homogenization theory, firstly proposed by Mei et al. (2011, 2014) and later extended by Liu et al. (2015) and Hu et al. (2021), was applied to study the effects of vegetation on waves.

Efforts have been made to predict the wave attenuation by different vegetation species without conducting a species-specific calibration of C_D. There are two aspects in this problem. One is to handle the vegetation flexibility effects and the other is to find a species-independent C_D relationship. Losada et al. (2016) followed Approach 3, but replaced h_v^* in Eq. (1) with the deflected plant length (l_D), which is defined as the actual length that is affecting the flow due to plant bending. l_D accounts for the flexibility effects, and is calculated as $l_D = l_0 \int_0^{l_D} \cos(\theta) dz$ in which l_0 is the physical plant height and θ is the bending angle relative to the vertical axis z. With $l_D/l_0 = 0.8$ and 0.6 for *P. maritima* in pure waves and wave–current scenarios, respectively, they determined empirical C_D formulas for pure regular/random waves and regular/random waves propagating with currents based on laboratory experiments involving real vegetation (Maza et al., 2015). Their work marks a progress in achieving a universal, species-independent C_D formula. However, the constant l_D/l_0 ratio in different waves introduces potential issues. Also, the determination of l_D requires the *a priori* measurements of vegetation postures, i.e., θ which is difficult to obtain in field experiments.

Recently, van Veelen et al. (2021) developed a mathematical model based on the Euler–Bernoulli beam theory for simulating the reconfiguration of stem posture and vegetation motions. With the vegetation flexibility effects handled by the mathematical model, van Veelen et al. (2021) predicted the damping of regular waves by rigid and flexible artificial vegetation along with real plants using the C_D formula from Hu et al. (2014). Lei and Nepf (2019) followed Approach 3, but replaced h_v^* in Eq. (1) with effective height, calculated from a scaling law. Later, Zhang et al. (2021) proposed a theoretical wave damping model for flexible vegetation, in which the drag induced by flexible vegetation was estimated with the scaling law. Both Lei and Nepf (2019) and Zhang et al. (2021) computed C_D from empirical formulas, $C_D = \max(1.95, 10KC^{-1/3})$ or $C_D = \max(1.0, 2.9KC^{-0.2})$, from Keulegan and Carpenter (1958) (KC is the Keulegan–Carpenter number), which were proposed for C_D of flat rigid plates or cylinders, respectively, in linear waves. The two C_D formulas in Keulegan and Carpenter (1958) may not be accurate for C_D of salt marshes under random wave conditions. In summary, a species-independent C_D formula for coastal wetlands in random wave environments is still missing.

This study aims to incorporate the influence of vegetation flexibility through effective plant height (EPH) and determine a species-independent C_D formula for salt marshes in random waves. The effective height, proposed and parameterized in Luhar and Nepf (2016), Luhar et al. (2017), Lei and Nepf (2019), Zhang et al. (2021), Zhang and Nepf (2021), is based on the assumption that flexible vegetation with physical height of l_0 generates the same drag as rigid vegetation with height of l_e. The l_e is considered as the effective height of flexible vegetation, which accounts for the effects of vegetation motion and deformation on reducing the vegetal drag. The scaling law is $l_e/l_0 = K(C_aL)^{-1/4}$, in which K is a scale coefficient, C_a is the Cauchy number, and L is the ratio between plant height and maximum water particle displacement A_w. The term C_aL describes the drag-to-stiffness ratio. The scaling of $l_e/l_0 \sim (C_aL)^{-1/4}$ is proven valid for $L \sim \mathcal{O}(1)$ (Luhar and Nepf, 2016; Lei and Nepf, 2019; Zhang et al., 2021). Luhar et al. (2017) firstly proposed $K = 2.25$ for seagrass blades in waves with $10^3 < C_aL < 10^4$. Later, Lei and Nepf (2019) extended the scaling law to a wider C_aL range from 0.3 to 2×10^4 and determined $K = 0.94$. Zhang et al. (2021) proposed $K = 1.2$ for cylindrical vegetation stems.

The present study is built upon the recent advance of the scaling law for flexible vegetation and high-quality measurements from field experiments and large-scale laboratory experiments that involve live vegetation. First, we calibrate C_D and best-fit a relationship between C_D and the Reynolds number (Re) based on a field dataset collected in Louisiana, USA during a tropical storm. The obtained $C_D - Re$ relationship is independent of vegetation flexibility because vegetation flexibility is separately accounted through the effective plant height. Then, we validate the universality of the proposed $C_D - Re$ relationship by applying it, along with the effective plant height, to two independent datasets that comprise different vegetation properties, especially rigidity and wave conditions. The validation results demonstrate that our proposed $C_D - Re$ formula avoids species dependence and can be applied across a wide range of wave conditions and vegetation properties whilst the flexibility effects are incorporated through the effective plant height. Finally, using the proposed C_D formula and effective plant height, we conservatively quantify the capacity of two typical salt marsh species: *Spartina alterniflora* and *Elymus athericus* for wave attenuation and shed light on the controlling factors of vegetation-induced wave attenuation.

2. Methods and data

2.1. Effective vegetation height and vegetation flexibility

For salt marsh vegetation that comprises a cylindrical stem and flat leaves, we measure the stem height (SH, denoted as $l_{0,s}$) as the length of the rigid stem portion from the plant base to the topmost node along the stem, and the total plant height (TPH, denoted as $l_{0,tot}$) as the distance from the plant base to the tip of the plant with all leaves aligned along the stem (Zhu and Chen, 2019a). The leaf height (LH, denoted as $l_{0,l}$) is the subtraction of SH from TPH for simplicity. Fig. 1a sketches SH, TPH and LH of a plant.

To implement the scaling law for the stem and leaves, we make the following assumptions: (1) each stem has n_l leaves; (2) leaves and stems are non-tapered; (3) leaves have uniform rectangular cross-section (width $b_{v,l}$ and thickness $t_{v,l}$) and Young's modulus Y_l; (4) stems have constant diameter $b_{v,s}$ and Young's modulus Y_s. The effective stem height (ESH, denoted as $l_{e,s}$) and effective leaf height (ELH, denoted as $l_{e,l}$) are determined through the scaling law (Lei and Nepf, 2019) based

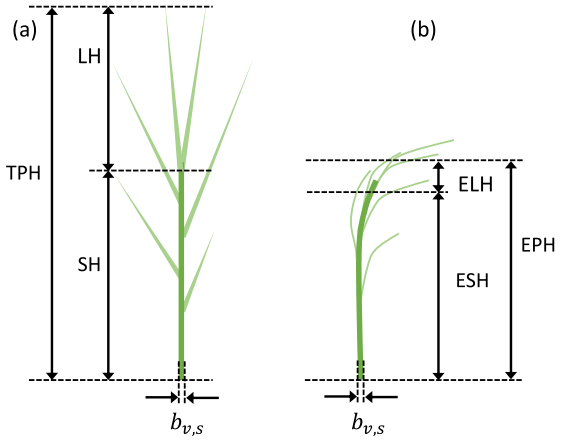

Fig. 1. (a) Sketch of physical vegetation heights, including stem height (SH), leaf height (LH) and total plant height (TPH). (b) Sketch of effective vegetation heights, including effective stem height (ESH), effective leaf height (ELH) and effective plant height (EPH). The stem diameter is $b_{v,s}$.

on their corresponding properties and physical heights ($l_{0,s}$ and $l_{0,l}$), respectively:

$$\frac{l_e}{l_0} = \min\left(K(C_aL)^{-1/4}, 1.0\right), \quad 0.3 < C_aL < 2\times 10^4 \tag{2}$$

and $K = 0.94$. For vegetation with $C_aL < 0.8$, the vegetation behaves like rigid vegetation and thus $l_e = l_0$ (Lei and Nepf, 2019; Zhang et al., 2021). The Cauchy number C_a is defined as below:

$$C_a = \frac{\rho b_v u^2 l_0^3}{YI} \tag{3}$$

in which, Y is the Young's modulus, I is the second moment of inertia, and u is the magnitude of characteristic horizontal velocity. Here, we determine u as the magnitude of the depth-averaged horizontal velocity over the submerged height of vegetation from linear wave theory: $u = \frac{H\sigma}{2\sinh kh}\frac{\sinh\min(kh,\ kl_{0,tot})}{\min(kh,\ kl_{0,tot})}$, in which H is the wave height, k is the wavenumber from the dispersion relationship based on linear wave theory, and σ is the wave angular frequency. The root-mean-square wave height H_{rms} and k_z and σ_z associated with mean wave period T_z are used for random waves. For emergent vegetation, $\min(kh,\ kl_{0,tot}) = kh$. For the vegetation stem with a cylindrical cross section, $I = \pi b_{v,s}^4/64$. For flat leaves, $I = b_{v,l}t_{v,l}^3/12$. The C_a and L for the stem and leaves are calculated separately using their respective properties. The subscripts 's' (for stem) and 'l' (for leaves) are omitted from Eqs. (2) and (3) for brevity. Fig. 1b sketches ESH and EBH of a plant.

Mullarney and Henderson (2010) proposed that the vegetation motions in waves are influenced by a combination of its Young's modulus, dimensions, and wave characteristics. They proposed a non-dimensional stiffness parameter S as below based on the Euler–Bernoulli equation (Karnovsky and Lebed, 2004) that balances the elastic restoring force and drag force,

$$S = \frac{Y(b_v/2)^3 T}{\rho C_D l_0^4 u} \tag{4}$$

In fact, $S = \frac{32\pi}{C_D}(C_aL)^{-1}$. The present study uses S to quantify the flexibility of vegetation.

2.2. Energy dissipation model

The spatial wave height distribution along a cross-shore transect is governed by the 1D energy balance equation:

$$\frac{\partial E_w C_g}{\partial x} = -\epsilon_v - \epsilon_b - \epsilon_f \tag{5}$$

in which E_w $(= \frac{1}{8}\rho g H_{\text{rms}}^2)$ is the wave energy density, C_g is the group velocity, the positive x-axis points in the onshore direction, and ϵ_v, ϵ_b and ϵ_f are the time-averaged energy dissipation rate per unit horizontal area induced by vegetation, wave breaking, and bottom friction, respectively. In this study, ϵ_f is modeled as below (e.g., Gon et al., 2020)

$$\epsilon_f = \frac{1}{2}\rho f_0 u_0^3 \tag{6}$$

in which f_0 is the bottom friction factor and u_0 is the maximum wave orbital velocity at bed. ϵ_b is modeled using empirical formulas proposed by Battjes and Stive (1985):

$$\epsilon_b = \frac{a\rho g Q H_b^2}{4T}, \quad \frac{Q-1}{\ln Q} = \left(\frac{H_{rms}}{H_m}\right)^2, \quad H_m = \frac{0.88}{k}\tanh\left(\frac{\xi kh}{0.88}\right) \tag{7}$$

in which a is an empirical coefficient ($a = 1$ in this study), g is the gravitational acceleration, $0 \le Q \le 1$ is the fraction of breaking waves, H_b is the height of the breaking wave, H_m is the local depth-limited wave height ($H_b = H_m$), ξ is the breaker ratio parameter with $H_m = \xi h$ in shallow water.

Regarding ϵ_v, Dalrymple et al. (1984) and Mendez and Losada (2004) proposed theoretical energy dissipation models as below for rigid vegetation:

$$\epsilon_v = \alpha\rho C_{D,s} b_{v,s} N_{v,s}\left(\frac{kg}{2\sigma}\right)^3 \frac{\sinh^3 kh_v + 3\sinh kh_v}{3k\cosh^3 kh} \tag{8}$$

in which $\alpha = \frac{2}{3\pi}H^3$ for regular waves and $\frac{1}{2\sqrt{\pi}}H_{rms}^3$ for random waves, h_v is vegetation height. Losada et al. (2016) adapted Eq. (8) for flexible vegetation applications by replacing h_v with the measured deflected vegetation height l_D. Luhar et al. (2017) substituted h_v with effective plant height. Lei and Nepf (2019) used the effective meadow height (see Eq. 19 in Lei and Nepf, 2019) in place of h_v.

Following Lei and Nepf's (2019) approach, we adjust h_v in Eq. (8) as follows:

$$h_v = \min\left(\frac{C_{D,l}b_{v,l}N_{v,l}}{C_{D,s}b_{v,s}N_{v,s}} \times l_{e,l} + l_{e,s},\ \ h\right) \tag{9}$$

For emergent vegetation, $h_v = h$. The first term in "$\min(\cdot,\cdot)$" represents the effective plant height (EPH), denoted as $l_{e,tot}$. The derivation of $l_{e,tot}$ expression is provided in Appendix A. The stem- and leaves-induced energy dissipation rates are modeled separately and combined into Eq. (8) through $l_{e,tot}$. The first term in $l_{e,tot}$ is related to leaves and the second term is related to the stem. Zhang et al. (2021) showed that $C_{D,l}/C_{D,s} \approx 2$ for $KC > 4$. For a plant that comprises a single stem and n_l leaves, Eq. (9) reduces to:

$$h_v = \min\left(2n_l l_{e,l}\frac{b_{v,l}}{b_{v,s}} + l_{e,s},\ \ h\right) \tag{10}$$

and thus $l_{e,tot} = 2n_l l_{e,l}\frac{b_{v,l}}{b_{v,s}} + l_{e,s}$. The number of leaves per stem (n_l) plays a role in $l_{e,tot}$ and affects ϵ_v. In the rest of the paper, we omit the subscript 's' from $C_{D,s}$ for brevity. This study uses T_z instead of the peak wave period (T_p) as the representative wave period. σ and k in Eqs. (7) and (8) are computed with T_z.

This study adopts the improved Euler finite difference method (Chaudhry, 1993) with second-order accuracy to solve Eq. (5) for spatial variations of wave heights. The incident wave conditions at the offshore boundary serve as boundary conditions. The grid spacing Δx is set as 0.05 m to balance the model accuracy and computational efficiency. The numerical solutions to Eq. (5) give the wave height attenuation induced by a combined effect of vegetation, wave breaking and bottom friction.

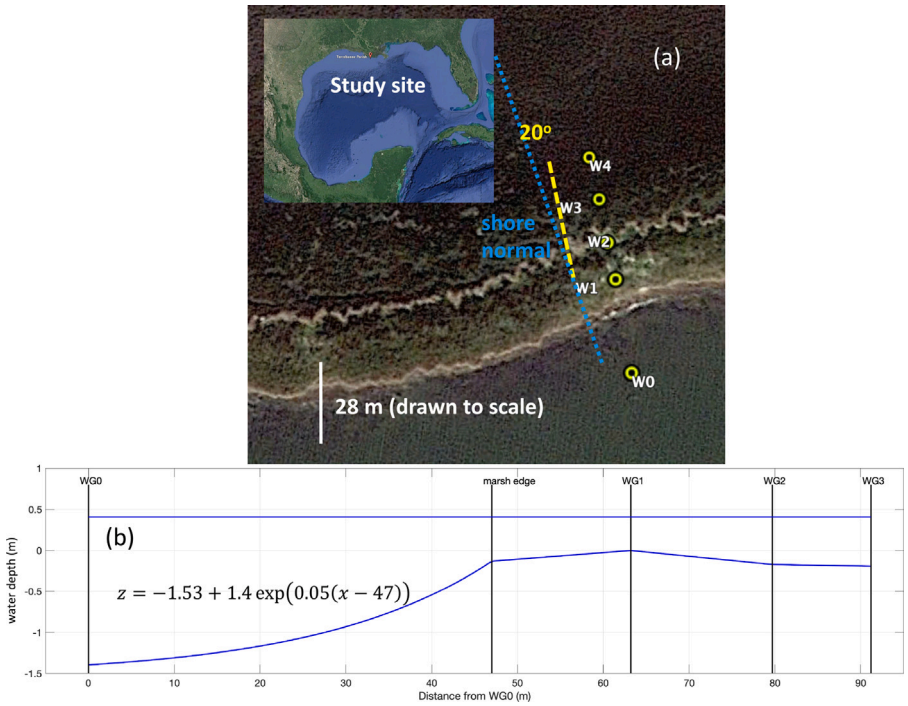

Fig. 2. (a) Aerial view of the study site and wave gage locations. Yellow dashed line shows the transect alignment. Blue dotted line shows the shore normal. (b) Water depth from W0 to W4.

2.3. Determination of $C_D - Re$ relationship

A field dataset, collected in upper Terrebonne Bay on the Louisiana coast of the Gulf of Mexico during Tropical Storm Lee (September 3–4, 2011), is used for determining the $C_D - Re$ relationship. This field dataset is denoted as the Gulf of Mexico (GoM) dataset. Five wave gages (W0–W4) were sampled continuously at 10 Hz over the 2-day duration of the storm. Gage W0 was located 45 m offshore, at a depth of 1.4 m below the mean sea level. Gage W1 was placed 16.2 m landward of the marsh edge. Different from Jadhav et al. (2013), the present study includes offshore W0 data and excludes W4 data because it recorded only a few bursts. The measured pressure data are re-analyzed with the Ocean Wave Analyzing Toolbox, OCEANLYZ (Karimpour and Chen, 2017). The GoM dataset contains a total of 276 wave measurements. The section between neighboring wave gages (i.e., W0–W1, W1–W2, W2–W3) is treated as one transect. Fig. 2a illustrates the layout of wave gages and orientations of transects. The transects have a bearing of 20° to the shore-normal. The wave travel distances between gages is overestimated by about 6% (= $1 - \cos(20°)$), introducing small errors to the estimated energy dissipation rate. Therefore, the wave obliquity and alongshore nonuniformity are negligible in the GoM dataset.

Because of the mild slope from W1 to W3, we linearly interpolate the water depth along onshore transects. The water depth profile between W0–W1 is determined by following the equilibrium profile (Wilson and Allison, 2008),

$$z = -1.53 + 1.4e^{0.05(x-47)} \tag{11}$$

in which x is the distance from W0 and z is the water depth. Both x and z are in meters. The W0–W1 data exhibits $4000 < Re < 5500$. The C_D in this Re range approaches the steady current limit $C_D = 1$ (Zhang et al., 2021; Keulegan and Carpenter, 1958). The coefficients in Eq. (11) are tuned to facilitate $C_D \approx 1.0$. Fig. 2b demonstrates the water depth profile.

This site is dominated by a common salt marsh species, *Spartina alterniflora*. Each plant consists of a relatively rigid stem and several flexible long leaves. The vegetation properties are averaged from 14 sample plants harvested at each transect. The field measurements (Jadhav, 2012; Jadhav et al., 2013) showed that $l_{0,s}/l_{0,tot} \approx 35\%$ and $Y_s = 80$ MPa. The Y_l was not measured. In the literature, Y_l of seagrasses, salt marshes, and artificial vegetation varies from 0.5 MPa to 4.8 GPa (Luhar and Nepf, 2016; Houser et al., 2015; Zhang et al., 2021). During the field visit, the *S. alterniflora* leaves were found easily bent to horizontal under moderate waves (Jadhav, 2012) while the stems stood upright. Therefore, we set $Y_l = 0.5$ MPa in the GoM dataset so that leaves have almost zero ELH during the storm. The effects of Y_l on ϵ_v will be discussed in Section 4.4. Tables 1 and 2 summarize the wave characteristics and vegetation properties of the GoM dataset.

Table 1
Wave characteristics (water depth h, incident root-mean-square wave heights $H_{rms,0}$ and mean wave period T_z) in three datasets.

		h (m)	$H_{rms,0}$ (m)	T_z (s)
GoM	W0–W1	1.75–2.25	0.31–0.58	2.5-4.0
	W1–W2	0.41–0.87	0.09–0.31	2.4-3.5
	W2–W3	0.44–1.01	0.02–0.21	2.4-4.8
USACE		0.30–0.53	0.03–0.14	1.0-1.9
North Sea	Irregular waves	2.0	0.20–0.87	1.7-5.0
	Regular waves	2.0	0.19–0.89	2.1-5.1

The steps below are followed to calibrate C_D for each wave condition:

1. Compute $l_{e,s}$ and $l_{e,l}$ from Eq. (2) using the wave characteristics at the leading edge of the vegetation field, and stem and leaf properties.
2. Compute h_v from Eq. (10).
3. Start with an initial $C_D = 1.0$. At each x grid, compute ϵ_v, ϵ_b and ϵ_f from Eqs. (8), (7), and (6), respectively ($\xi = 0.8$ and $f_0 = 0.015$ (Gon et al., 2020), see B for fractions of energy dissipation rate at all transects), solve Eq. (5) for H_{rms} using the improved Euler method, and iteratively calibrate C_D using the bisection method until the relative difference between the observed and modeled H_{rms} is less than 2%.

Table 2
Vegetation properties (stem height $l_{0,s}$, leaf height $l_{0,l}$, total plant height $l_{0,tot}$, stem diameter $b_{v,s}$, leaf width $b_{v,l}$, leaf thickness $t_{v,l}$, stem population density $N_{v,s}$, numbers of leaves per stem n_l, Young's modulus of stem Y_s, Young's modulus of leaf Y_l) in the three independent datasets and from Chatagnier (2012).

	$l_{0,s}$ (m)	$l_{0,l}$ (m)	$l_{0,tot}$ (m)	$b_{v,s}$ (mm)	$b_{v,l}$ (mm)	$t_{v,l}$ (mm)	$N_{v,s}$ (stems/m^2)	n_l (leaves)	Y_s (MPa)	Y_l (MPa)
GoM	0.21 0.23	0.518 0.518	0.62 0.63	8.0 7.5	4.36	0.685	400 420	5	80	**0.5***
USACE	0.41	/	0.41	6.4	/	/	200, 400	/	172.4	/
North Sea	0.7	/	0.7	1.3	/	/	1225	/	2696	/
Chatagnier (2012)	0.28	/	0.28	8.0	/	/	247	/	160	/

***Estimated values.**

The calibrated C_D are best fit to a formula in the format of $C_D = a + \left(\frac{b}{Re}\right)^c$, where $a,\ b,\ c$ are parameters of the best fit curve. Re is defined as $Re = \frac{\rho b_v u_b}{\mu}$ with μ is the dynamic viscosity of water, and u_b is the maximum near-bed orbital velocity at the leading edge of vegetation $u_b = \frac{H_{rms,\text{edge}}\sigma_z}{2}\frac{1}{\sinh k_z h}$, in which $H_{rms,\text{edge}}$ is H_{rms} at the leading edge.

2.4. Validating the universality of $C_D - Re$ relationship

After obtaining the $C_D - Re$ relationship from Section 2.3, we apply it to two independent datasets to prove its universality. These datasets are: (i) the USACE (United States Army Corps of Engineers) dataset, laboratory experiments carried out at the U.S. Army Engineer Research and Development Center with vegetation mimics made of polyolefin tubing (Anderson and Smith, 2014); and (ii) the North Sea dataset, laboratory experiments conducted in the Large Wave Flume in Germany using transplanted natural *Elymus athericus* from North Sea coasts (Möller et al., 2014). The wave height distributions are modeled by following the steps as below:

1. Obtain incident wave conditions including H_{rms}, T_z, and h.
2. Obtain stem and leaves morphology and biomechanical properties including $l_{0,s}$, $l_{0,l}$, $b_{v,s}$, $b_{v,l}$, $t_{v,l}$, n_l, Y_s, and Y_l.
3. Compute $l_{e,s}$ and $l_{e,l}$ from Eq. (2) using wave conditions at the leading edge of the vegetation field, and stem and leaf properties.
4. Compute h_v from Eq. (10), Re from its definition, and C_D from the proposed $C_D - Re$ relationship.
5. At each x grid, compute ϵ_v, ϵ_b and ϵ_f from Eqs. (8), (7), and (6), respectively, and solve Eq. (5) for wave heights using the improved Euler method.

For Step 1, we re-analyze the raw wave measurements of the USACE datasets with MACE (a MATLAB toolbox for Coastal Engineer, MACE, 2009). According to data availability, T_z is calculated through wave-by-wave analysis or approximated from T_p as below:

$$T_z = \begin{cases} \overline{T_i} & \text{USACE} \\ T_p/1.25 & \text{North Sea (irregular waves)} \end{cases} \tag{12}$$

in which T_i is the zero-upcrossing period, '$\overline{\cdot}$' denotes averaging process. $T_z = T_p/1.25$ holds for the JONSWAP-type spectra with a peak enhancement factor of 3.3 (Goda, 2000). Table 1 lists the wave characteristics in these datasets.

For Step 2, Table 2 lists the vegetation properties in these datasets.

For Step 5, when resolving ϵ_f, f_0 is set as 0.15 for the USACE dataset to reach good agreement with measured H_{rms} in their control tests that involve no vegetation. The TRANSPOR program (van Rijn, 1993) also confirms that f_0 in the USACE dataset is as high as 0.15. For the North Sea dataset, f_0 is set as 0.015 to reach good agreement with measured H_{rms} in their 'mowed' tests where vegetation is cut. We enforce $\epsilon_b = 0$ in the North Sea and USACE datasets because they both experimented on non-breaking waves.

Jadhav et al. (2013), Anderson and Smith (2014), and Möller et al. (2014) also proposed empirical C_D formulas based on the GoM, USACE, and North Sea datasets, respectively. Their C_D formulas and treatments of h_v are considered as baseline models:

Baseline model 1: (Jadhav et al., 2013)

$$h_v = l_{0,s}$$

$$C_D = 0.36 + \frac{2600}{Re},\ 600 < Re < 3200 \tag{13}$$

where $Re = \frac{\rho b_v u_b}{\mu}$ and u_b is the maximum near-bed orbital velocity from linear wave theory using H_{rms} and T_p.

Baseline model 2: (Anderson and Smith, 2014)

$$h_v = l_{0,tot}$$

$$C_D = 0.11 + \left(\frac{2067.7}{Q_{Re}}\right)^{0.64},\ 533 < Re < 2296 \tag{14}$$

where $Q_{Re} = \frac{Re}{(l_{0,tot}/h)^{1.5}}$, $Re = \frac{\rho b_v u_b}{\mu}$ and u_b is the maximum horizontal velocity at the top of stems from linear wave theory using H_{rms} and T_p.

Baseline model 3: (Möller et al., 2014)

$$h_v = l_{0,tot}$$

$$C_D = 0.159 + \left(\frac{227.3}{Re}\right)^{1.615},\ 17 < Re < 1170 \tag{15}$$

where $Re = \frac{\rho b_v u_b}{\mu}$ and u_b is the maximum near-bed orbital velocity in front of vegetation from linear wave theory using H_{rms} and T_p.

In these baseline models, Re is defined differently and hence applicable at varying ranges. The performance of baseline models is evaluated based on their capability in predicting the wave attenuation of independent datasets. The model performance is quantified with the normalized root-mean-square difference (NRMSE), defined as below:

$$\text{NRMSE} = \frac{\sqrt{\frac{1}{M}\sum_{i=1}^{M}(X_i^{\text{pre.}} - X_i^{\text{obs.}})^2}}{\frac{1}{M}\sum_{i=1}^{M} X_i^{\text{obs.}}} \tag{16}$$

in which, M is the number of observations in a dataset, and the superscripts 'pre.' and 'obs.' denote predictions and observations, respectively. Variable X represents either the wave height or the wave height reduction rate.

2.5. Numerical experiments for quantifying wetland capacity in wave attenuation

After validating the universality of the proposed $C_D - Re$ relationship, we conduct numerical experiments to quantify the capacity of two representative salt marshes, *S. alterniflora* and *E. athericus*, for

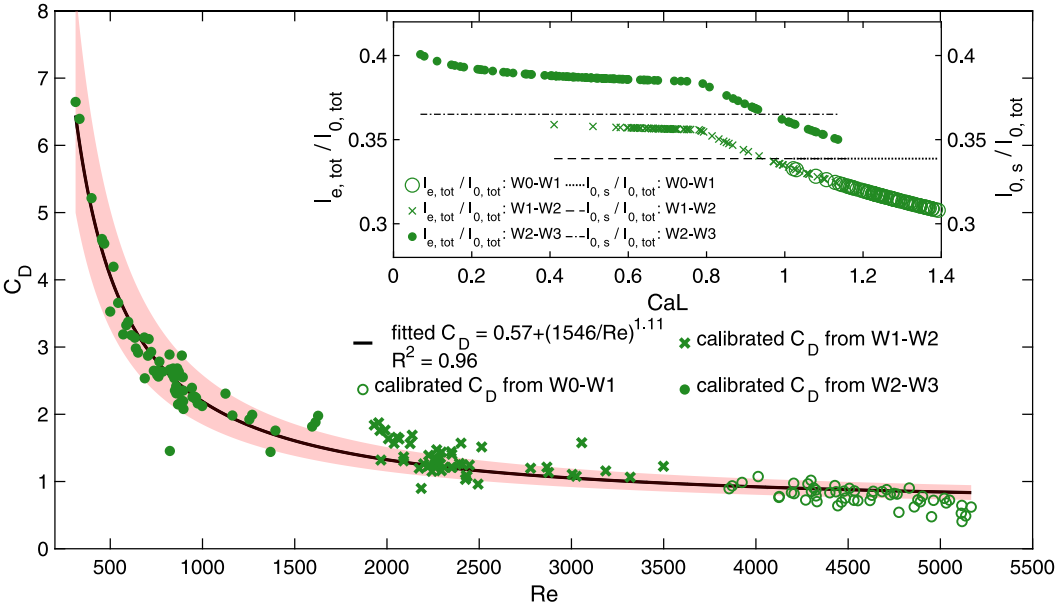

Fig. 3. Calibrated drag coefficient C_D of Gulf of Mexico dataset collected during Tropical Storm Lee (green symbols), the fitted $C_D - Re$ curve (black line), and 95% confidence interval for $C_D - Re$ relationship (red shade). Inset: variations of the effective plant height to total plant height ratio with CaL, together with the stem height to total plant height ratio.

wave attenuation under varying wave conditions. In the numerical experiments, the steps in Section 2.4 are followed to compute the wave attenuation. Approximately 308,000 non-breaking wave conditions are tested: (i) $0.01 \le H_s/h \le 0.6$; (ii) $-3.8 \le \log_{10}(h/gT_z^2) \le -0.7$; and (iii) $T_z = 3-12$ s. Wave breaking criteria (Kamphuis, 1991) are applied to filter out breaking incident wave conditions. A 50-m long vegetation field with fixed biomechanical properties is placed on a flat bottom with constant water depth. The numerical experiments can provide insight into intertwined factors that control the wave attenuation.

S. alterniflora is commonly observed in intertidal wetlands in Atlantic and Gulf coasts of the United States. In the numerical experiments, the biomechanical properties of *S. alterniflora*, listed in Table 2, come from a field survey conducted in Louisiana by Chatagnier (2012). *E. athericus* is typical in intertidal wetlands in southern North Sea coasts of Europe and has spread to European salt marshes in the last decade. The biomechanical properties of *E. athericus* in the numerical experiments are the same as in the North Sea dataset. Considering that leaf properties, especially Y_l, are uncertain and the stem-induced energy dissipation rate is dominant, we omit leaves in the numerical experiments by setting $n_l = 0$ and present a conservative evaluation of wetland capacity in wave attenuation.

3. Results

3.1. A unified drag coefficient relationship

The inset in Fig. 3 presents the ratios of $l_{e,tot}/l_{0,tot}$ and $l_{0,s}/l_{0,tot}$. At the most seawards transect W0–W1, under large incident waves, we have $l_{e,l}/l_{0,l} = 2\%$, $l_{e,s}/l_{0,s} = 86\% - 93\%$, and $l_{e,tot}/l_{0,tot} = 31\% - 33\%$. These ratios describe that vegetation leaves are bent to almost horizontal to the ground and the stems are slightly deformed. When waves propagate to the most shorewards transect W2–W3, the incident wave heights become significantly smaller. At W2–W3, stems stay almost upright ($l_{e,s}/l_{0,s} \ge 91\%$) and leaves are still largely deflected ($l_{e,l}/l_{0,l} \approx 2\% - 4\%$). This small $l_{e,l}$ is consistent with field observations that the leaves were easily bent to horizontal under even moderate waves (Jadhav, 2012).

The difference between EPH and TPH ($l_{e,tot}/l_{0,tot} \approx 35\%$) is attributed to vegetation flexibility, mostly the leaf flexibility. C_D determined based on EPH becomes independent of flexibility. Moreover, because $l_{0,s} \approx l_{e,tot} (\approx 35\% l_{0,tot})$, it is pragmatic to use SH as a substitute of EPH for *S. alterniflora* in Louisiana coast.

Fig. 3 also shows the calibrated C_D, varying with Re, along the three transects. The scatter in C_D is mostly attributed to the spatial variability in plant biomechanical properties and uncertainties in natural environments (e.g., existence of weak currents). The best-fit C_D curve as below has the coefficient of determination $R^2 = 0.96$.

$$C_D = 0.57 + \left(\frac{1546}{Re}\right)^{1.11}, \quad 312 \le Re \le 5164 \tag{17}$$

3.2. Universality of the proposed $C_D - Re$ relationship

Eq. (17) is validated against two independent datasets, whose vegetation sampling locations, types and stem rigidity are shown in Fig. 4a. Among the two datasets and the GoM dataset, *E. athericus* in the North Sea dataset is the most flexible ($0.06 \le S \le 0.10$), whereas *S. alterniflora* in the GoM dataset is the most rigid ($63 \le S \le 157$).

Fig. 4b shows that vegetation stems in the three datasets exhibits different extents of deformation ($l_{e,s} = 1/7 l_{0,s}$ for *E. athericus*, $l_{e,s} = l_{0,s}$ for *S. alterniflora*) because of different flexibility, which is indicated by $(C_aL)^{-1}$ (small C_aL means rigid and large C_aL means flexible). Lei and Nepf (2019) exhibited that the scaling law falls within 95% confidence interval of their experiment measurements for vegetation with moderate and low stiffness ($1 < C_aL < 10,000$). Therefore, our estimated $l_{e,s}$ has a high level of accuracy.

The predicted wave heights, obtained by following steps in Section 2.4, achieve good agreement with observations (Figs. 4c and 4d) for the two independent datasets with $R^2 \ge 0.93$ and NRMSE ≤13%. Define the wave height reduction rate as:

$$\gamma = 1 - \frac{H_{rms}}{H_{rms,0}} \tag{18}$$

The predicted γ also exhibits good agreement with observations in all datasets with $R^2 = 0.97$, NRMSE = 13% (Fig. 4f). Excellent agreement for the GoM dataset is expected because it is used to determine proposed $C_D - Re$ formula.

Some North Sea cases have Re as small as 54, which exceeds the lower bound of Re (i.e., $Re \ge 312$) of Eq. (17). However, the model-data comparisons for those cases with $54 \le Re \le 312$ have $R^2 = 0.91$ and 0.92 for regular and irregular waves, respectively. It indicates that

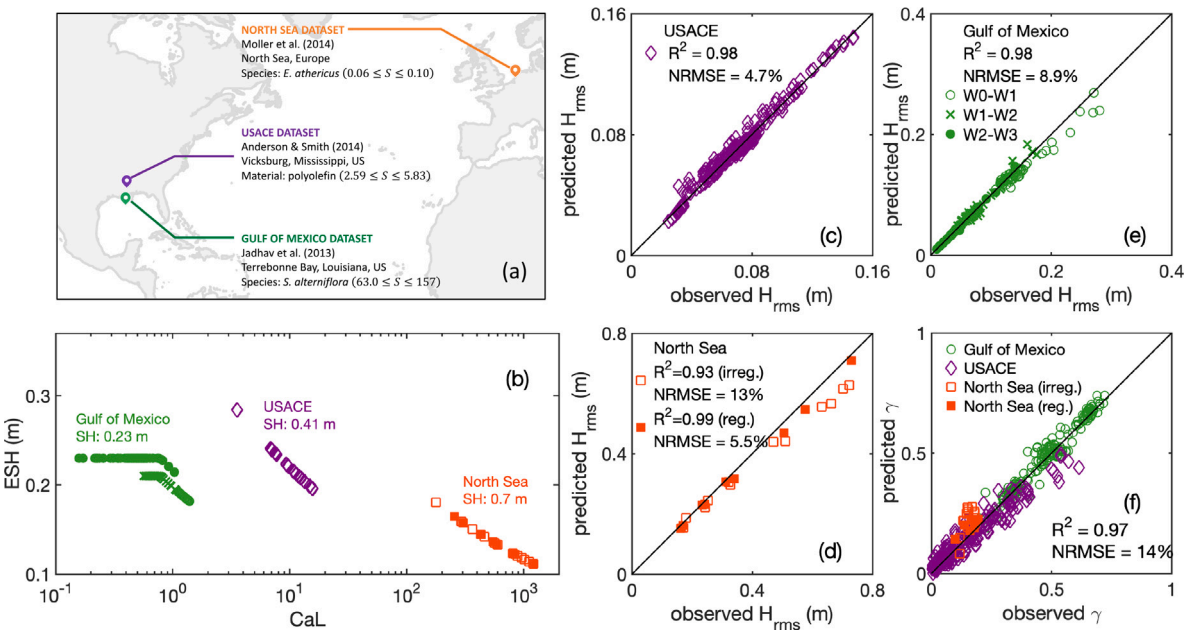

Fig. 4. (a) Locations, vegetation types and dimensionless stiffness parameters in the three independent datasets. (b) Effective stem height $l_{e,s}$ in the three independent datasets. Comparisons of observed and predicted root-mean-square wave heights for (c) the USACE dataset; (d) the North Sea dataset; and (e) the Gulf of Mexico dataset. The 'irreg.' and 'reg.' in (d) represent irregular and regular wave cases, respectively. (f) Comparisons of observed and predicted wave height reduction rate, γ.

the applicable Re range of Eq. (17) can be extended to $54 \le Re \le 5164$ and the C_D range to $0.8 \le C_D \le 45$. The broad Re range covers a large variety of field-scale waves. The upper bound of Re has practical meanings because during extreme events such as Hurricane Katrina, Re can be as large as 7100 (Chen et al., 2008).

We now summarize the treatment of h_v, definition of Re, and the C_D formula for wave height prediction in the present study as follows:

$$h_v = \min\left(2n_l l_{e,l}\frac{b_{v,l}}{b_{v,s}} + l_{e,s},\ \ h\right)$$

$$C_D = 0.57 + \left(\frac{1546}{Re}\right)^{1.11}, \quad 54 \le Re \le 5164 \tag{19}$$

where $Re = \frac{\rho b_v u_b}{\mu}$ and u_b is the maximum near-bed orbital velocity in front of vegetation from linear wave theory using H_{rms} and T_z.

The three baseline models are applied to all datasets and their model-data comparisons are shown in Fig. 5. To make fair comparisons, we calculate h_v, Re and C_D in the same way as the baseline models do. The scatter plots of γ in Fig. 4f and Fig. 5 demonstrate that the proposed $C_D - Re$ formula, used together with EPH, outperforms all baseline models in terms of wave height prediction. The model performance, quantified with NRMSE of γ, is summarized in Table 3. The gray table cells highlight the datasets that were used to obtain the C_D formulas in baseline models. The excellent agreement in model-data comparisons from the present study relies on a key factor: vegetation flexibility effects are taken into accounted through EPH, so C_D is independent of vegetation flexibility. By contrast, the existing C_D formulas in baseline models were determined based on the physical height of vegetation, either SH or TPH. Vegetation flexibility effects are aggregated into their C_D formulas, which tend to be species-specific. For instance, Baseline Model 2 overpredicts γ in the GoM and North Sea datasets, in which vegetation has different orders of magnitude of stiffness (Fig. 5b). Our proposed $C_D - Re$ formula unifies these empirical C_D formulas for salt marshes, and is applicable to C_aL ranging from 0.1 to 1000.

3.3. Capacity of wetlands for wave attenuation

The validated $C_D - Re$ formula allows us to evaluate the capacity of salt marshes in wave attenuation with high confidence. Numerical

Table 3
Performance (NRMSE) of the present study and baseline models in predicting γ for different datasets.

	Present study	Baseline model 1	Baseline model 2	Baseline model 3
GoM	6%	**8%**	31%	38%
USACE	30%	113%	**30%**	84%
North Sea (irreg.)	56%	344%	99%	**25%**

experiments, as introduced in Section 2.5, are conducted. The results reveal that the wave height reduction rate γ is primarily determined by two dimensionless parameters: relative wave height ($H_{rms,0}/h$) and effective submergence ($l_{e,tot}/h$). The latter incorporates vegetation flexibility effects. Numerical results regarding $l_{e,tot}$, γ and C_D are synthesized and presented through different layers in Fig. 6.

The solid lines in Fig. 6 show the variations between $l_{e,tot}$ and $H_{rms,0}$ with fixed h (= 3, 2, 1 and 0.5 m) and T_z (= 5 s). Attributed to its large stem stiffness, *S. alterniflora* stems stay upright in a shallow water depth ($h = 0.5$ m), while slightly deform in an intermediate water depth ($h = 3$ m) under large $H_{rms,0}$. By contrast, *E. athericus* experiences large deformations in shallow and intermediate water depths under moderate $H_{rms,0}$.

The red dotted lines in Fig. 6 illustrate the variations of C_D. *E. athericus* induces larger C_D than *S. alterniflora*, because *E. athericus* stem is four times thinner, which results in much smaller Re under the same wave conditions. C_D in an *E. athericus* field is more sensitive to the wave environment because C_D increases exponentially as Re decreases, especially when Re is smaller than 1000.

By omitting ϵ_b and ϵ_f in Eq. (5), the wave height at x m away from leading edge of vegetation field can be theoretically expressed as below by following (Mendez and Losada, 2004),

$$H(x) = \frac{H_0}{1 + K_D H_0/2x} \tag{20}$$

$$K_D = \alpha^* C_D b_{v,s} N_{v,s} k \frac{\sinh^3 kh_v + 3\sinh kh_v}{(\sinh 2kh + 2kh)\sinh kh} \tag{21}$$

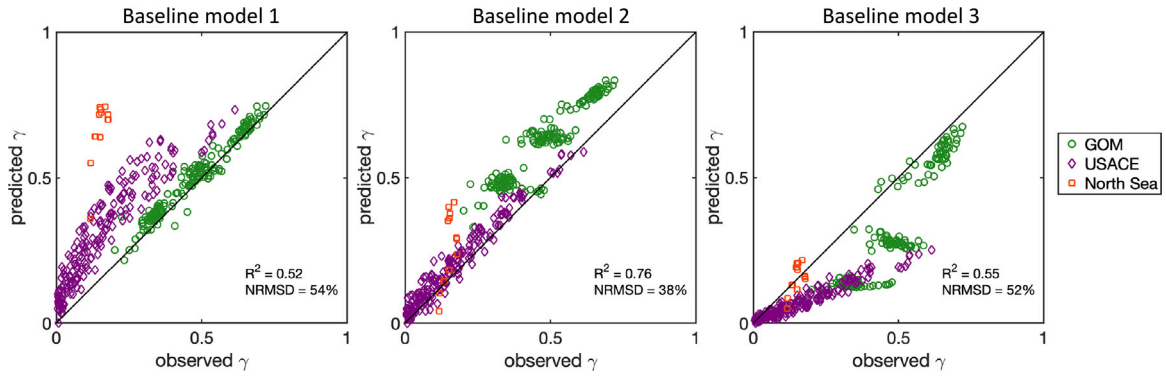

Fig. 5. Comparisons of observed and predicted wave height reduction rate, γ, using three baseline models.

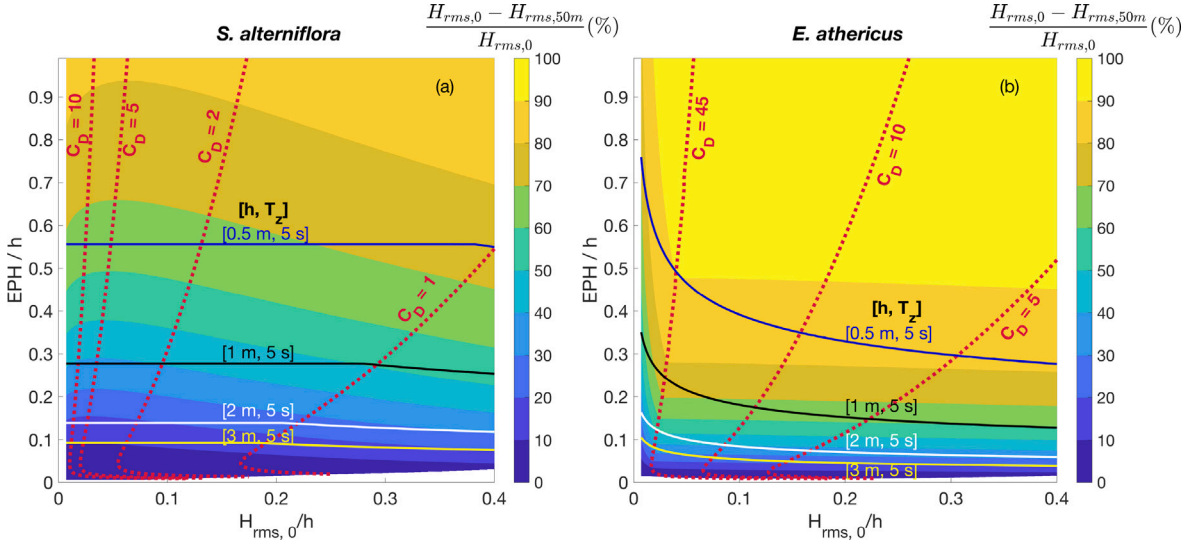

Fig. 6. Contour lines of drag coefficient C_D (red dashed lines), and variations of wave height reduction rate with relative wave height ($H_{rms,0}/h$) and effective submergence ($l_{e,tot}/h$) (background contour plot) for waves with varying water depth and wave height, and a fixed mean wave period of 5 s . Variations of $l_{e,tot}/h$ with $H_{rms,0}/h$ for waves with fixed mean wave period of 5 s in water with depth of 0.5 m, 1 m, 2 m and 3 m (blue, black, white and yellow lines, respectively). Results in presence of two typical salt marshes: (a) *Spartina alterniflora*, and (b) *Elymus athericus* are shown.

in which, $\alpha^* = \frac{8}{9\pi}$ for regular waves and $\frac{2}{3\sqrt{\pi}}$ for random waves (Eqs. 8 and 30 in Mendez and Losada (2004)). With the approximation of

$$\sinh^3 kh_v + 3\sinh kh_v \approx kh_v,\ \sinh 2kh + 2kh \approx kh,\ \sinh kh \approx kh \tag{22}$$

we obtain

$$\gamma \propto K_D H_0 \propto C_D \frac{kH_0}{kh}\frac{kh_v}{kh} = C_D \frac{H_0}{h}\frac{h_v}{h} \tag{23}$$

Fig. 7 shows the contour lines of γ for $T_z = 3-12$ s. These overlapping contour lines suggest that γ is not sensitive to T_z within the range of 3 ~ 12 s. For *S. alterniflora*, C_D mildly varies from 0.8 to 5 (red dotted lines in Fig. 6a), so γ mainly depends on H_0/h and h_v/h. For deep water waves, the approximations in Eq. (22) do not hold. This explains the non-converging contour lines of $\gamma = 20\%$ in Fig. 7a. For *E. athericus*, C_D rapidly changes from 1 to 45 (red dotted lines in Fig. 6b), and thus γ is essentially a function of C_D, H_0/h, and h_v/h. C_D is a function of Re, which depends on u_b. With the fixed T_z and H_0, Re decreases as kh decreases. The response of C_D to Re is more dramatic in shallow water. This explains the non-converging contour lines of $\gamma > 80\%$ in Fig. 7b.

Because γ is insensitive to T_z within the range of 3 ~ 12 s, we draw the contour plot of γ for waves with fixed $T_z = 5$ s as the background layers of Fig. 6. For waves with T_z from 3 s to 12 s, γ can be determined from $H_{rms,0}/h$ and $l_{e,tot}/h$ from background layers in Fig. 6. For instance, in shallow water ($h = 0.5$ m, $T_z = 5$ s, solid blue lines), *S. alterniflora* ($\gamma = 60\% - 80\%$) attenuates less incoming waves than *E. athericus* ($\gamma > 80\%$). In an intermediate water depth ($h = 3$ m, $T_z = 5$ s, solid yellow lines), *S. alterniflora* and *E. athericus* induce $\gamma \approx 10\%$ for large waves. If stem deformation is not considered for *E. athericus* (i.e., $l_{e,tot}/h$ remains unchanged as $H_{rms,0}$ increases), γ would be overestimated by 10% and 30% in shallow and intermediate water depths, respectively. In other words, *E. athericus* field may lose up to 30% wave attenuation capacity once bent. To avoid unrealistically large C_D values corresponding to small Re, C_D is capped by 45, which is the upper bound of C_D (see Section 3.2). This upper limit of C_D causes the sharp bend in the contour plot for small waves with $H_{rms,0}/h < 0.05$ in Fig. 6b.

In presence of *S. alterniflora*, wave attenuation is enhanced as $H_{rms,0}/h$ increases from 0.05 to 0.4, although C_D and EPH slightly drop (Fig. 6a). This correlation between γ and $H_{rms,0}/h$ aligns with laboratory observations (Anderson and Smith, 2014). However, large incident waves may not always experience greater γ, especially in highly flexible vegetation. In *E. athericus*, wave attenuation drops as $H_{rms,0}/h$ increases from 0.05 to 0.4. The considerable reduction in EPH and C_D counteracts the effect of an increase in incident wave height. In Fig. 10, we only plot $l_{e,tot}/h$ from 0 to 1 because when $l_{e,tot}/h > 1.0$, the emergent part does not contribute to the wave attenuation. In other words, γ induced by vegetation with $l_{e,tot}/h > 1.0$ is equivalent to γ induced by vegetation with $l_{e,tot}/h = 1.0$.

Fig. 8 demonstrates the variations of γ with h and significant wave height (H_s) for $T_z = 5$ s. For instance, for *S. alterniflora* in a 3 m deep

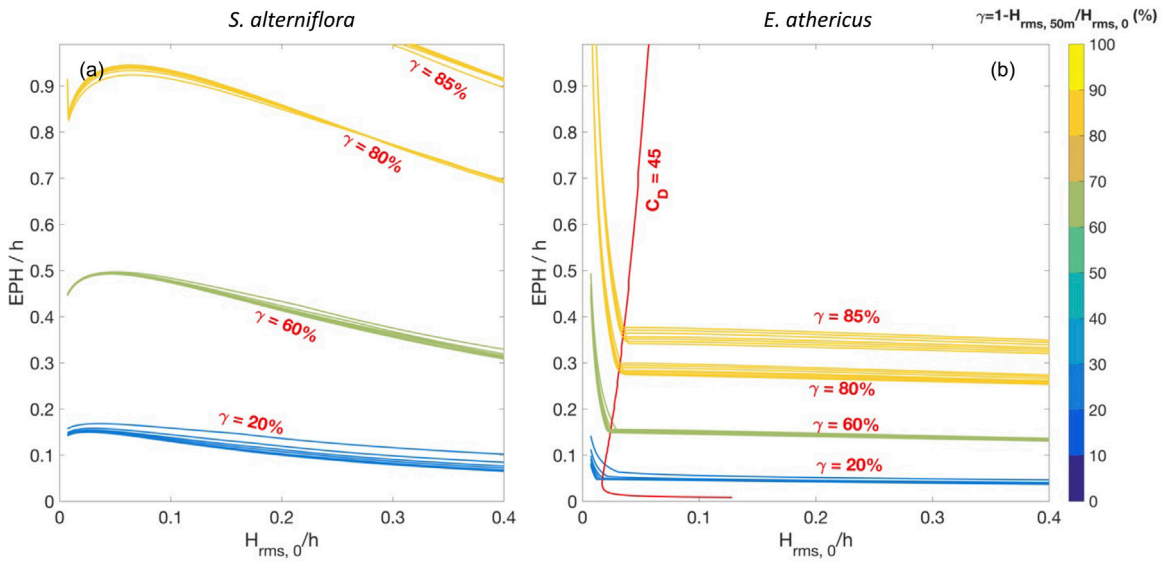

Fig. 7. Contour lines of wave height reduction rate γ for mean wave period $T_z = 3 - 12$ s.

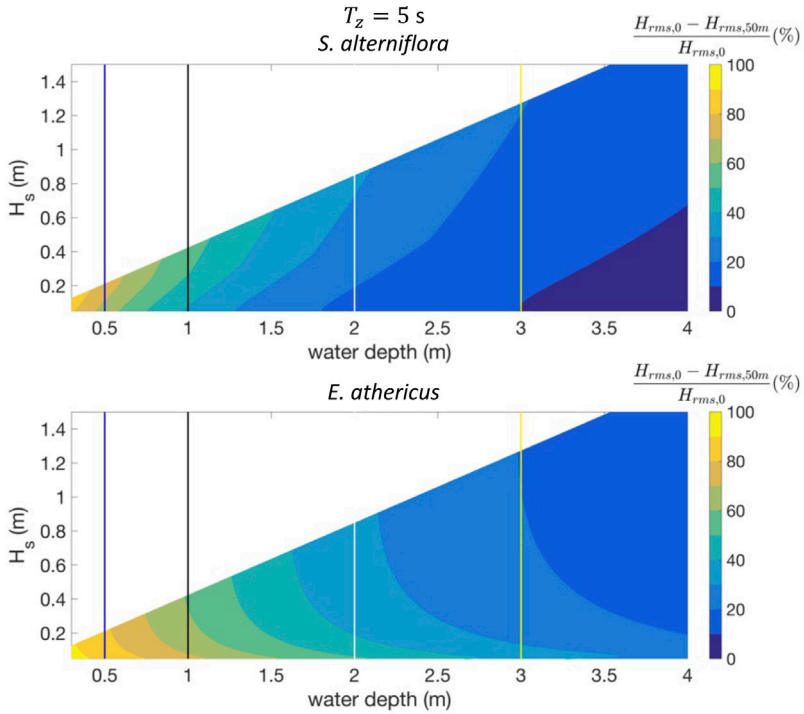

Fig. 8. Contour plot of wave height reduction rate γ for waves with mean wave period $T_z = 5$ s. Vertical lines correspond to water depth h of 0.5 m (blue), 1 m (black), 2 m (white), and 3 m (yellow), respectively.

water, γ increases from 10% to 20% as H_s increases from 0.05 m to 1.2 m. The orientation of the contour lines of γ illustrates that wave attenuation increases as wave height increases. However, for *E. athericus*, the contour lines of γ has an opposite orientation, suggesting that wave attenuation decreases as wave height increases. For *E. athericus* in a 3 m deep water, γ decreases from 30% to 20% as H_s increases from 0.05 m to 1.2 m.

4. Discussion

4.1. The scaling law

The scaling law in Eq. (2) was proposed based on the assumptions: (1) moderate wave excursions ($L \sim \mathcal{O}(1)$) (Luhar and Nepf, 2016; Lei and Nepf, 2019); and (2) a balance between the vegetal drag and the restoring force due to elasticity. The latter assumption constrains the application of the scaling law. Once the buoyancy (measured by a dimensionless buoyancy parameter β in Henderson (2019)) dominates the restoring force, the stem configurations and the scaling law would be altered. Our results show that Eq. (2) is applicable to the GoM and USACE datasets because $L \sim \mathcal{O}(1) - \mathcal{O}(10)$, and their buoyancy is negligible ($|\beta/S| \ll 1$ and $S \gg 1$). In the North Sea dataset ($\beta/S = 0.32$ and $\beta/\sqrt{S} \approx 0.1$), the vegetal drag is balanced out by elasticity and a small but non-negligible buoyancy. Nevertheless, the contribution of buoyancy to EPH, governed by β^2/S (Henderson, 2019), is limited because $\beta^2/S \approx 0.01$.

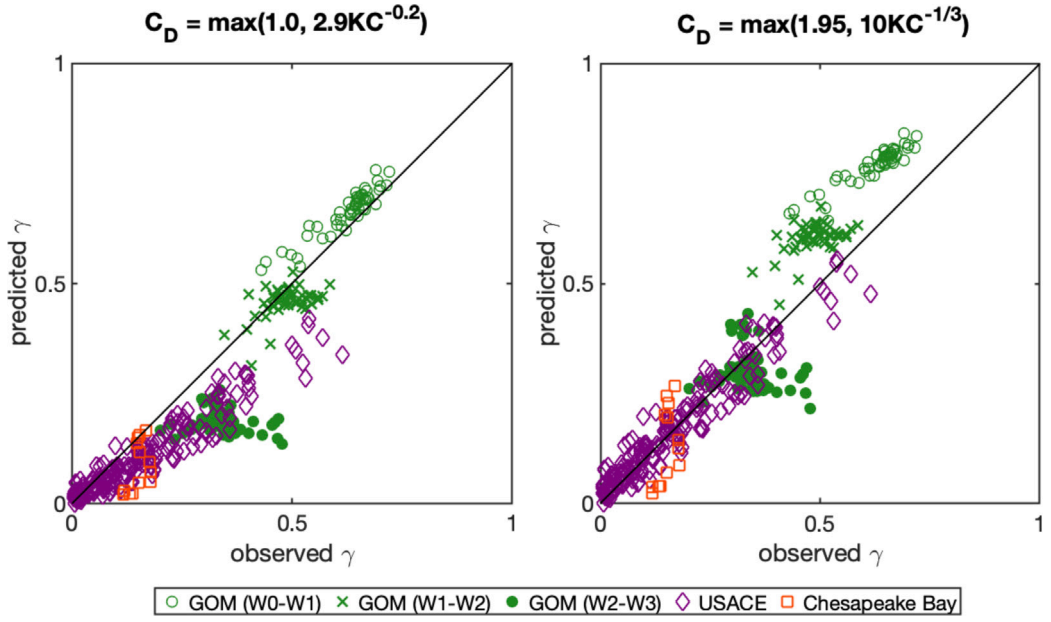

Fig. 9. Comparisons of the observed and modeled wave attenuation rate (γ). The modeled γ is obtained by following steps in Section 2.4 using C_D from (a) $C_D = \max(1.0, 2.9KC^{-0.2})$ proposed by Keulegan and Carpenter (1958) for cylinders in linear waves and (b) $C_D = \max(1.95, 10KC^{-1/3})$ proposed by Keulegan and Carpenter (1958) for flat plates in linear waves.

C_D was omitted in the scaling law assuming that C_D remains nearly constant (Luhar and Nepf, 2016; Lei and Nepf, 2019; Zhang et al., 2021). However, C_D can span across orders of magnitude (e.g., C_D varies from 2 to 42 in the North Sea dataset), it is necessary to involve C_D in the scaling law. Balancing the vegetal drag and elasticity yields $EIA_w/l_e^3 \sim C_D \rho b_v l_e u^2$, we get a modified scaling law as $l_e/l_0 \sim (C_D \cdot C_a L)^{-1/4}$. Nevertheless, including C_D in the scaling law only slightly improves the wave height comparisons in Fig. 4d.

4.2. Spatial variations of C_D

When modeling the wave decay by vegetation, most models use a bulk C_D, calculated based on Re in the front of the vegetation field, for the whole transect. The H_{rms}, Re and C_D vary with distance into the wetlands. The use of Re at the leading edge of the vegetation field for C_D calculation may lead to an underestimation of wave attenuation. Considering that our C_D formula is determined based on averagely 15-m long transects of the GoM dataset, we suggest dividing the long stretch of wetland in practical applications into segments with length of $\mathcal{O}$(10 m), and use a bulk C_D and h_v for each segment.

4.3. Comparison of the present study, Lei and Nepf (2019) and Zhang et al. (2021)

Lei and Nepf (2019) (denoted as "LN2019") and Zhang et al. (2021) (denoted as "ZLN2021") also implemented the scaling law to model wave damping by flexible vegetation. The present study is aimed at finding a general $C_D - Re$ formula that can be applied in wave damping models that use an effective plant height, whereas LN2019 and ZLN2021 were focused on demonstrating the effectiveness of the scaling law and the concept of effect height in predicting wave decay over a meadow of flexible vegetation, including leaves, using the existing C_D formulas. Because of different objectives, LN2019 and ZLN2021 used existing empirical C_D formulas: $C_D = \max(1.95, 10KC^{-1/3})$ or $C_D = \max(1.0, 2.9KC^{-0.2})$ from Keulegan and Carpenter (1958), which were proposed for C_D of flat rigid plates or cylinders, respectively, in linear waves. Fig. 9 shows that neither C_D formulas from Keulegan and Carpenter (1958), used together with EPH, can accurately predict

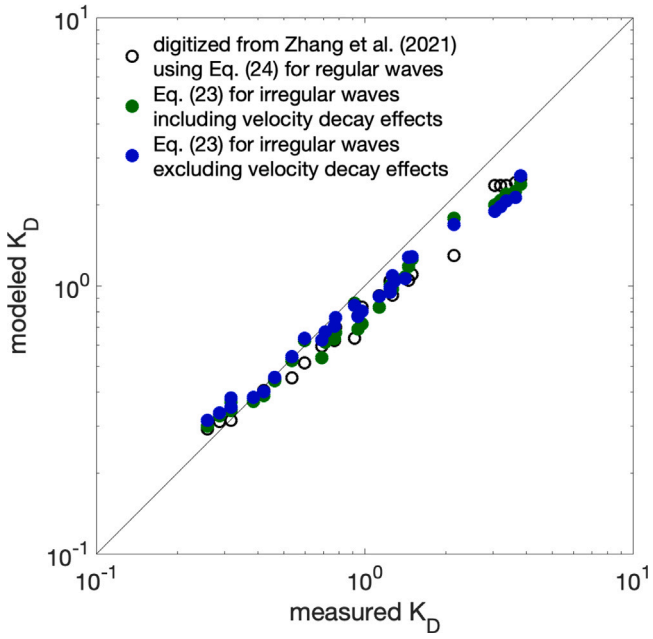

Fig. 10. Comparisons of wave damping coefficient K_D using Eqs. (21) and (24). The effect of the horizontal velocity decay within the vegetation canopy on wave damping is illustrated by the blue and green symbols.

the damping of random waves in salt marshes under the field and lab conditions considered in this study.

Based on the definition (Luhar and Nepf, 2016) that effective height l_e is the height of a rigid, upright vegetation that generates the same horizontal drag as the flexible vegetation of height l_0, LN2019 and the present study replace the drag by flexible vegetation with the drag by rigid vegetation with the height of l_e, and derive a theoretical wave height in vegetation as in Eq. (20) with $h_v = l_{e,tot}$ in Eq. (21). The derivation exactly follows (Mendez and Losada, 2004) with ϵ_b and ϵ_f omitted. The vegetation motions and reconfiguration are accounted by letting $h_v = l_{e,tot}$. ZLN2021 applied the scaling law to F_d/F_r throughout

the wave cycle (i.e., $F_d/F_r = K(CaL)^{-1/4}$) in which, F_d and F_r are the drag on the flexible vegetation and on an equivalent rigid vegetation, respectively, and got a different expression of K_D,

$$K_D = \frac{8}{9\pi} k \frac{\sinh^3 kl_{0,s} + 3\sinh kl_{0,s}}{(\sinh 2kh + 2kh)\sinh kh} N_{v,s} \times \left(\frac{l_{0,l}}{l_{0,s}} n_l C_{D,l} b_{v,l} K_l (Ca_l L_l)^{-1/4} + C_{D,s} b_{v,s} K_s (Ca_s L_s)^{-1/4} \right) \quad (24)$$

ZLN2021 pragmatically used $l_{0,s}$ in the numerator in Eq. (24) to represent the stem and leaves of the equivalent rigid vegetation. In ZLN2021, LN2019 and the present study, the leaf- and stem-induced energy dissipation rate are estimated separately. Both Eq. (21) with $h_v = l_{e,tot}$ and Eq. (24) contain the leaf and stem effects. Owing to the Taylor expansion of $\sinh y = y + \mathcal{O}(\frac{y^3}{3!})$ and $\sinh^3 y = \frac{\sinh 3y - 3\sinh y}{4}$, K_D in Eqs. (21) and (24) converge as $kl_{0,s}$ approaches zero. Eqs. (21) and (24) can be used interchangeably for shallow water waves ($kh < 0.1\pi$), although the K_D expression in ZLN2021 (Eqs. 14-16 in Zhang et al. (2021)) needs to be modified as below for random wave applications,

$$K_D = \frac{2}{3\sqrt{\pi}} k \frac{\sinh^3 kl_{0,s} + 3\sinh kl_{0,s}}{(\sinh 2kh + 2kh)\sinh kh} N_{v,s} \times \left(\frac{l_{0,l}}{l_{0,s}} n_l C_{D,l} b_{v,l} K_l (Ca_l L_l)^{-1/4} + C_{D,s} b_{v,s} K_s (Ca_s L_s)^{-1/4} \right) \quad (25)$$

The present study does not involve the damping of horizontal velocity within the vegetation canopy and the drag reduction due to the sheltering effect in a meadow. The omittance of these two processes leads to small differences in wave damping predictions for vegetation with $N_{v,s} = 400$ stems/m^2 as shown in Fig. 10.

4.4. Leaf contribution to wave attenuation

The contribution of leaves to wave damping is controlled by the leaf-related term $2n_l \frac{b_{v,l}}{b_{v,s}} l_{e,l}$ in h_v (Eq. (10)), which is largely dependent on the leaf rigidity. Zhang et al. (2021) used $Y_l = 0.37$ GPa in a field application and demonstrated that the leaves of *S. alterniflora* play an important role in wave attenuation. The present study assumes $Y_l = 0.5$ MPa and find that $l_{e,l}$ is almost zero and leaves do not induce comparable wave attenuation as stems. To investigate the effects of Y_l on wave attenuation, we compute $l_{e,l}$, ϵ_v and H_{rms} of the GoM W1–W2 dataset with $Y_l = 0.5$ MPa and 0.37 GPa, respectively. Considering that our C_D formula is determined with $Y_l = 0.5$ MPa, we use $C_D = \max(1.0, 2.9KC^{-0.2})$ as in Zhang et al. (2021) rather than our $C_D - Re$ relationship. Although $C_D = \max(1.0, 2.9KC^{-0.2})$ is not appropriate for random waves, it still helps predict γ reasonably well for the GoM W1–W2 dataset (Fig. 9 Left).

Fig. 11 shows that $l_{e,l}/l_{e,tot}$ is almost zero when $Y_l = 0.5$ MPa and increases to around 11% when $Y_l = 0.37$ GPa. The larger $\int \epsilon_v dx$ and wave damping when $Y_l = 0.37$ GPa are attributed to the greater $l_{e,l}$. The differences between H_{rms} modeled with the two Y_l values reveal the wave damping caused by rigid leaves with $Y_l = 0.37$ GPa. Fig. 11 further proves that Y_l in the GoM dataset must be orders of magnitude smaller than Y_l used in Zhang et al. (2021). $Y_l = 0.5$ MPa is a reasonable assumption for the GoM dataset because it leads to better agreement with observed H_{rms} than $Y_l = 0.37$ GPa. With $Y_l = 0.5$ MPa, we find that leaves do not play an important role in wave attenuation in the GoM dataset. For better quantification of leaf contribution to wave attenuation, we suggest collecting Y_l, $b_{v,l}$, $t_{v,l}$, n_l in field experiments.

4.5. Predicting wave attenuation with limited vegetation measurements

Vegetation properties are essential for predicting the wave attenuation. However, these data, especially of leaves, are usually not collected in field experiments. Here, we provide an example case for predicting wave attenuation with limited vegetation measurements. Garzon et al. (2019) collected wave attenuation data in *S. alterniflora* in Eastern Shore of Chesapeake Bay, United States. They measured $N_{v,s} = 319$ stems/m^2, $b_{v,s} = 5.5$ mm and $l_{0,tot} = 0.68$ m. For the remaining vegetation properties, reasonable assumptions and approximations are desired. For $l_{0,s}$, Chatagnier (2012) reported that $l_{0,s}/l_{0,tot} \approx 0.4$ based on field surveys in Louisiana. The GoM dataset shows $l_{0,s}/l_{0,tot} = 0.34 - 0.36$. Therefore, we take the average of the reported $l_{0,s}/l_{0,tot}$ ratios and assume $l_{0,s}/l_{0,tot} = 0.37$. The Y_s is estimated as 200 MPa based on an empirical relationship of $Y_s = 473253(l_{0,s}/b_{v,s})^{1.5943}$ (Y_s in MPa, and $l_{0,s}$ and $b_{v,s}$ in m) by Chatagnier (2012). The leaf properties are assumed the same as in the GoM dataset (Table 2). Fig. 12 shows that the modeled H_{rms} (following steps in Section 2.4) achieves good agreement with measurements. For improved quantification of stem and leaf contribution to wave attenuation, we suggest collecting both stem and leaf properties in field experiments.

4.6. Limitations of the work

It is worth pointing out that some simplified, pragmatic treatments of vegetation parameters have been used in order to obtain the $C_D - Re$ relationship. In particular, n_l is treated as a constant, and the geometry and modulus of elasticity of the stem and leaves are assumed to be uniform although these parameters vary spatially and temporally in nature. The performance of the proposed $C_D - Re$ relationship is bounded by these simplifications. For highly tapered stems and leaves, or for a vegetation patch whose n_l has significant deviation from the mean value, or for vegetation with uncertain stem/leaf measurements, the C_D value determined from the proposed $C_D - Re$ relationship may not lead to an accurate prediction of wave height decay in vegetation.

Additionally, the effects of leaves are neglected in the numerical experiments. As shown in Zhang et al. (2021) and Section 4.4, stiff leaves with large Y_l can play an important role in wave dissipation. Section 3.3 only demonstrates a conservative evaluation of wetland capacity in wave attenuation. Moreover, the proposed $C_D - Re$ relationship is applicable to a range of wave/vegetation conditions with $0.1 < C_aL < 1000$. The proposed C_D formula needs to be further validated once field/laboratory data beyond this applicable range becomes available.

4.7. Future work

In practical applications, spatially and seasonally varying C_D and h_v are desired to reflect the gradient of plant dimensions, flexibility, and wave conditions from low marsh to high marsh and from growing season to dormant season. The performance of our proposed $C_D - Re$ relationship in quantifying the spatial and seasonal variations of wave attenuation requires further evaluation. Field surveys need to be conducted to collect: (1) wave attenuation from low marsh to high marsh, and spatial distributions of vegetation properties across low marsh species to high marsh species; (2) wave attenuation and plant biomechanical properties at different stages of the life-cycle of salt marshes.

It has been observed in multiple hurricanes that if the bottom shear stress during a storm exceeds the soil strength, wetland root systems will be uprooted or swept away, similar to what occurred in the upper Breton Sound estuary in the Mississippi River Delta after Hurricane Katrina (Howes et al., 2010; Vuik et al., 2018). Pre- and post-storm wave and vegetation data are needed to evaluate the performance of our proposed $C_D - Re$ in quantifying the changes of wetlands' wave attenuation capacity after extreme events.

The breakage or damage of vegetation is not modeled in Fig. 6. Continuous bending of stems could lead to toppling (90° bending angle) and stem breakage (Silinski et al., 2015; Vuik et al., 2018), and eventually lead to aboveground biomass removal and reduce the wetland capacity in wave energy dissipation. Modeling the failing point of wetland vegetation relies on accurate calculation of the drag force. Field data are required to evaluate the performance of the proposed $C_D - Re$ formula in estimating the vegetal drag force for the modeling of stem breakage.

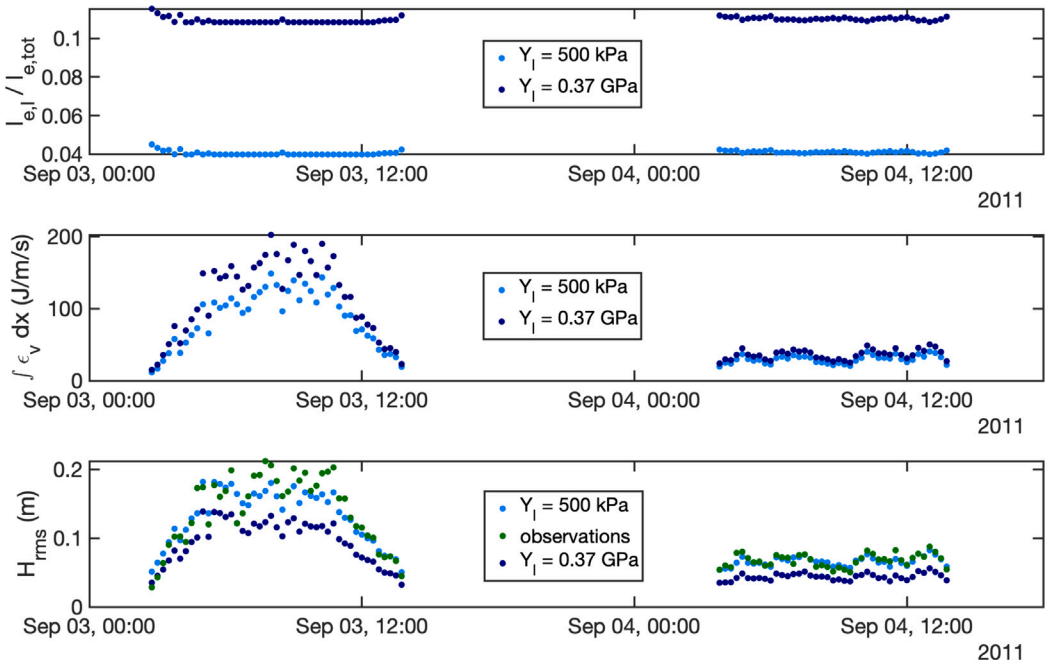

Fig. 11. The fractions of effective leave height in effective total height, integrated vegetation-induced energy dissipation rates, and wave heights of the GoM W1–W2 dataset with Young's modulus of leaves of 0.37 GPa (dark blue symbols) and 500 kPa (light blue symbols), respectively.

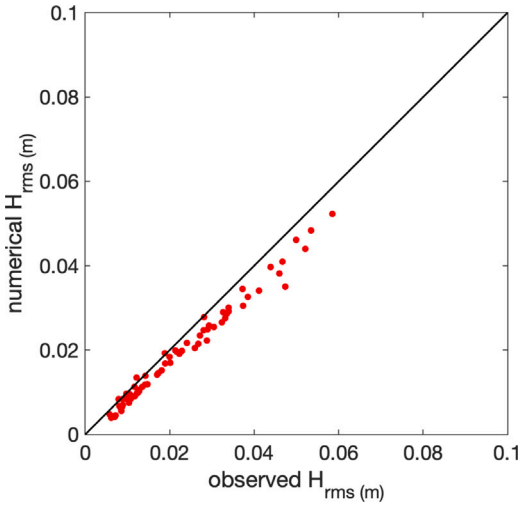

Fig. 12. Comparisons of modeled and observed wave heights for dataset in Garzon et al. (2019).

5. Conclusions

With the vegetation flexibility effects separately accounted for through the effective plant height (EPH), a species-independent $C_D - Re$ relationship is presented based on a field dataset collected from a site dominated by *Spartina alterniflora* in Louisiana, USA during a tropical storm. The proposed $C_D - Re$ relationship, used together with the EPH from the scaling law, is proven to consistently and accurately reproduce wave attenuation in two independent datasets that involve vegetation with different flexibility and random waves of diverse conditions. The proposed $C_D - Re$ relationship provides an important closure model for quantifying wave attenuation in response to vegetation with species-specific biomechanical properties, as well as wave forcing. The proposed $C_D - Re$ formula facilitates coastal communities making informed decisions in implementing NNBFs and optimizing hybrid approaches of hard and natural infrastructure to increase coastal resilience. The key findings are as follows:

- The proposed $C_D - Re$ relationship in Eq. (19), used together with h_v defined in Eq. (10), leads to good agreement between modeled and measured wave height reduction rates ($R^2 = 0.97$, NRMSE = 13%) for flexible vegetation with $0.1 < CaL < 10^3$. The proposed $C_D - Re$ relationship has a wide applicable range of Re from 54 to 5164.
- The wave height reduction rate γ is primarily determined by two dimensionless parameters: relative wave height ($H_{rms,0}/h$) and effective submergence ($l_{e,tot}/h$). With a fixed water depth, for relatively stiff salt marsh species like *S. alterniflora*, γ increases as $H_{rms,0}$ increases. In contrast for highly flexible salt marsh species like *E. athericus*, γ decreases as $H_{rms,0}$ increases.
- The contribution of leaves to wave attenuation is largely dependent on Young's modulus of the leaf Y_l. For *S. alterniflora*, this study shows that leaves with $Y_l = 0.5$ MPa do not induce large wave attenuation in the GoM dataset. However, if Y_l increases to 0.37 GPa as suggested in Zhang et al. (2021) for saltmarshes in New England, USA, the contribution of leaves are not negligible. We recommend that leaf biophysical properties be collected in future field experiments.
- The proposed C_D formula can be leveraged to quantify the capacity of coastal wetlands in wave attenuation. Fig. 6 provides an estimate of γ by two typical salt marsh species in waves with T_z ranging from 3 s to 5 s. The wetland capacity in wave attenuation shown in Fig. 6 is conservative because leaves are omitted due to uncertainties in Y_l and leaf dimensions. The performance of the proposed C_D formula needs to be further evaluated with field data collected at different stages of vegetation life cycle and more vegetation species.

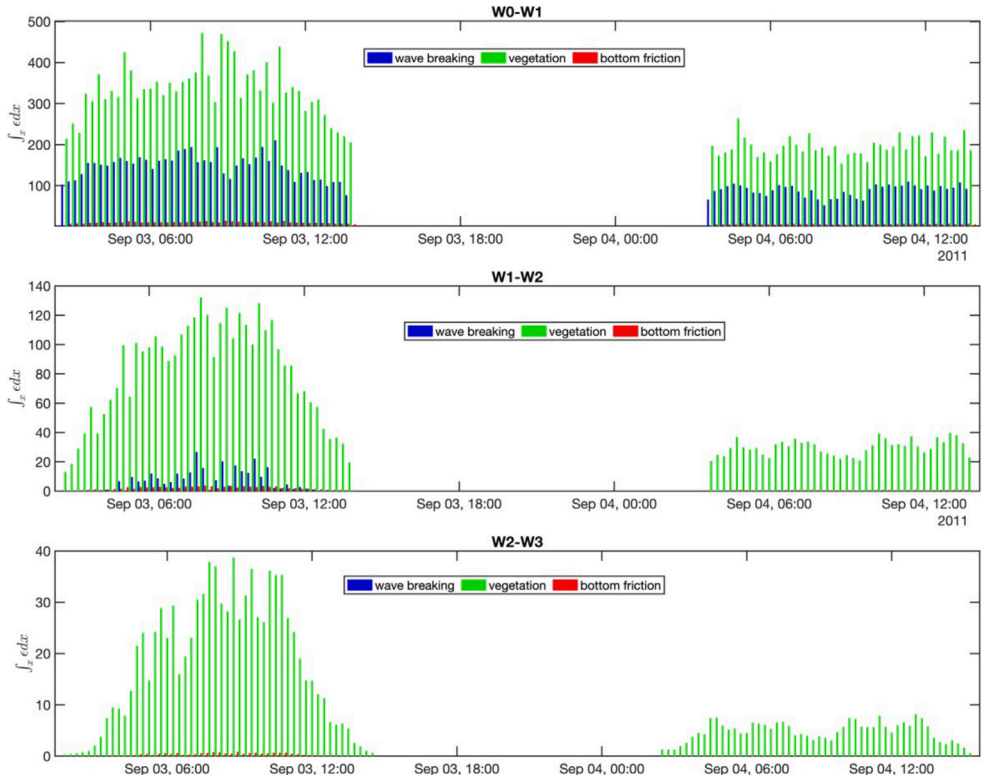

Fig. B.13. Time series of energy dissipation rate due to wave breaking, vegetation, and bottom friction in the GoM dataset.

CRediT authorship contribution statement

Ling Zhu: Performed research, Wrote the paper, Reviewed the manuscript. **Qin Chen:** Performed research, Wrote the paper, Reviewed the manuscript. **Yan Ding:** Analyzed data, Reviewed the manuscript. **Navid Jafari:** Wrote the paper, Reviewed the manuscript. **Hongqing Wang:** Analyzed data, Reviewed the manuscript. **Bradley D. Johnson:** Analyzed data, Reviewed the manuscript.

Declaration of competing interest

The authors declare that they have no known competing financial interests or personal relationships that could have appeared to influence the work reported in this paper.

Data availability

Data will be made available on request.

Acknowledgments

This research was funded by the USACE, USA Flood and Coastal Systems Program (W912HZ-16-2-0025) and the U.S. Coastal Research Program (W912HZ-20-2-0046). Additional support was provided in part by the U.S. National Science Foundation (Grant #2139882, #2139883) and NFWF, USA (Project #55032). H. Wang was partially supported by the U.S. Geological Survey (USGS) Ecosystems Mission Area. We thank Dr. Celso Ferreira, Mary Anderson Bryant, and Dr. Iris Moller for sharing their valuable datasets. We thank Dr. Julie D. Rosati (USACE) and Dr. Davina L. Passeri (USGS) for reviewing our paper and providing suggestions. We thank both anonymous reviewers for their insightful comments and suggestions. Any use of trade, firm, or product names is for descriptive purposes only and does not imply endorsement by the U.S. Government.

Appendix A. Derivation of Eq. (9)

Based on the definition of ϵ_v as in Eq. (1), we have,

$$\epsilon_v = \int_{-h}^{-h+l_{e,s}} C_{D,s} b_{v,s} N_{v,s} u^2 |u| dz + \int_{-h+l_{e,s}}^{-h+l_{e,s}+l_{e,l}} C_{D,l} b_{v,l} N_{v,l} u^2 |u| dz \quad \text{(A.1)}$$

The two terms on the right hand side represent the stem- and leaf-induced energy dissipation rate, respectively. Assuming small vertical variations of u in the leaf-occupied water column ($-h + l_{e,s} \le z \le -h + l_{e,s} + l_{e,l}$), we can simplify the above equation to,

$$\begin{aligned}
\epsilon_v &= \int_{-h}^{-h+l_{e,s}} C_{D,s} b_{v,s} N_{v,s} u^2 |u| dz + C_{D,l} b_{v,l} N_{v,l} u_l^2 |u_l| l_{e,l} \\
&= \int_{-h}^{-h+l_{e,s}} C_{D,s} b_{v,s} N_{v,s} u^2 |u| dz + C_{D,s} b_{v,s} N_{v,s} u_l^2 |u_l| l_{e,l}^* \\
&= \int_{-h}^{-h+l_{e,s}} C_{D,s} b_{v,s} N_{v,s} u^2 |u| dz + \int_{-h+l_{e,s}}^{-h+l_{e,s}+l_{e,l}^*} C_{D,s} b_{v,s} N_{v,s} u^2 |u| dz \\
&= \int_{-h}^{-h+l_{e,s}+l_{e,l}^*} C_{D,s} b_{v,s} N_{v,s} u^2 |u| dz \quad \text{(A.2)}
\end{aligned}$$

in which, $u \approx u_l$ in the leaf-occupied water column, and $l_{e,l}^* = \frac{C_{D,l} b_{v,l} N_{v,l}}{C_{D,s} b_{v,s} N_{v,s}} l_{e,l}$. Inserting the theoretical expression of u from linear wave theory into Eq. (A.2), we get the expression of ϵ_v in Eq. (8) and h_v in Eq. (9).

Appendix B. Energy dissipation rates of the GoM dataset

In the GoM dataset, ϵ_v, ϵ_b and ϵ_f are modeled separately. Bar plots in Fig. B.13 show the time series of ϵ_b, ϵ_v and ϵ_f along the three transects. W0–W1 contains significant wave breaking, leading to ϵ_b = 30% of total energy dissipation rate (ϵ_{tot}). Gage W1 is intentionally placed far away from the breaking zone at the marsh edge. Along W1–W2, ϵ_b is at most 16%ϵ_{tot}. Along W2–W3, ϵ_b is negligible.

References

Anderson, M., Smith, J., 2014. Wave attenuation by flexible, idealized salt marsh vegetation. Coast. Eng. 83, 82–92.

Augustin, L.N., Irish, J.L., Lynett, P., 2009. Laboratory and numerical studies of wave damping by emergent and near-emergent wetland vegetation. Coast. Eng. 56 (3), 332–340.

Battjes, J.A., Stive, M.J.F., 1985. Calibration and verification of a dissipation model for random breaking waves. J. Geophys. Res.: Oceans 90, 9159–9167.

Chakrabarti, A., Chen, Q., Smith, H.D., Liu, D., 2016. Large Eddy simulation of unidirectional and wave flows through vegetation. J. Eng. Mech. 142 (8), 04016048.

Chatagnier, J., 2012. The Biomechanics of Salt Marsh Vegetation Applied to Wave and Surge Attenuation Master thesis. Louisiana State University.

Chaudhry, M.H., 1993. Open-Channel Flow. Prentice Hall, Englewood Cliffs, NJ.

Chen, Q., Wang, L., Tawes, R., 2008. Hydrodynamic response of northeastern Gulf of Mexico to hurricanes. Estuar. Coasts 31 (6), 1098–1116. http://dx.doi.org/10.1007/s12237-008-9089-9.

Chen, Q., Zhao, H., 2012. Theoretical models for wave energy dissipation caused by vegetation. J. Eng. Mech. 138, 221–229.

Dalrymple, R.A., Kirby, J.T., Hwang, P.A., 1984. Wave diffraction due to areas of energy dissipation. J. Waterw. Port Coast. Ocean Eng. 110, 67–79.

del Valle, A., Eriksson, M., Ishizawa, O.A., 2020. JJ Miranda, mangroves protect coastal economic activity from hurricanes. Proc. Natl. Acad. Sci. 117, 265–270.

Duarte, C., Losada, I., Hendriks, I., Mazarrasa, I., Marba, N., 2013. The role of coastal plant communities for climate change mitigation and adaptation. Nat. Clim. Change 3, 961–968.

Editorial, 2021. Valuing wetlands. Nat. Geosci. 14, 111. http://dx.doi.org/10.1038/s41561-021-00713-4.

Fagherazzi, S., 2014. Storm-proofing with marshes. Nat. Geosci. 7, 701–702.

Ganju, N.K., Defne, Z., Kirwan, M.L., Fagherazzi, S., D'Alpaos, A., Carniello, L., 2017. Spatially integrative metrics reveal hidden vulnerability of microtidal salt marshes. Nature Commun. 8 (14156).

Garzon, J.L., Maza, M., Ferreira, C.M., Lara, J.L., Losada, I.J., 2019. Wave attenuation by Spartina saltmarshes in the chesapeake bay under storm surge conditions. J. Geophys. Res.: Oceans 124, 5220–5243.

Goda, Y., 2000. Random seas and design of maritime structures. Adv. Ser. Ocean Eng. 33.

Gon, C.J., MacMahan, J.H., Thornton, E.B., Denny, M., 2020. Wave dissipation by bottom friction on the inner shelf of a rocky shore. J. Geophys. Res.: Oceans 125, e2019JC015963.

Henderson, S., 2019. Motion of buoyant, flexible aquatic vegetation under waves: simple theoretical models and parameterization of wave dissipation. Coast. Eng. 152, 103497.

Hochard, J.P., Hamilton, S., Barbier, E.B., 2019. Mangroves shelter coastal economic activity from cyclones. Proc. Natl. Acad. Sci. 116, 12232–12237.

Houser, C., Trimble, S., Morales, B., 2015. Influence of leaf flexibility on the drag coefficient of aquatic vegetation. Estuaries Coasts 38, 569–577.

Howes, N.C., FitzGerald, D.M., Hughes, Z.J., Georgiou, I.Y., Kulp, M.A., Miner, M.D., Smith, J.M., Barras, J.A., 2010. Hurricane-induced failure of low salinity wetlands. Proc. Natl. Acad. Sci. 107, 14014–14019.

Hu, K., Chen, Q., Wang, H., 2015. A numerical study of vegetation impact on reducing storm surge by wetlands in a semi-enclosed estuary. Coast. Eng. 95, 66–76.

Hu, J., Mei, C.C., Chang, C.W., Liu, P.L-F., 2021. Effect of flexible coastal vegetation on waves in water of intermediate depth. Coast. Eng. 168, 103937.

Hu, Z., Suzuki, T., Tjerk, Z., Wim, U., Stive, M., 2014. Laboratory study on wave dissipation by vegetation in combined current–wave flow. Coast. Eng. 88, 131–142.

Jadhav, R.S., 2012. Field Investigation of Wave and Surge Attenuation in Salt Marsh Vegetation and Wave Climate in a Shallow Estuary (Ph.D. Dissertation). Louisiana State University.

Jadhav, R.S., Chen, Q., Smith, J.M., 2013. Spectral distribution of wave energy dissipation by salt marsh vegetation. Coast. Eng. 77, 99–107.

Jongman, B., 2018. Effective adaptation to rising flood risk. Nature Commun. 9 (1986).

Kamphuis, J.W., 1991. Wave transformation. Coast. Eng. 15 (3), 173–184.

Karimpour, A., Chen, Q., 2017. Wind wave analysis in depth limited water using oceanlyz, a Matlab toolbox. Comput. Geosci. 106 (181).

Karnovsky, I.A., Lebed, O.I., 2004. Free Vibrations of Beams and Frames: Eigenvalues and Eigenfunctions. McGraw!Hill, New York.

Keulegan, G., Carpenter, L., 1958. Forces on cylinders and plates in an oscillating fluid. J. Res. Natl. Bur. Stand. 60, 423–440.

Lei, J., Nepf, H., 2019. Wave damping by flexible vegetation: Connecting individual leaf dynamics to the meadow scale. Coast. Eng. 147, 138–148.

Leonardi, N., Ganju, N.K., Fagherazzi, S., 2016. A linear relationship between wave power and erosion determines salt-marsh resilience to violent storms and hurricanes. Proc. Natl. Acad. Sci. 113, 64–68.

Liu, P.L-F., Chang, C.W., Mei, C.C., Lomonaco, P., Martin, F.L., Maza, M., 2015. Periodic water waves through an aquatic forest. Coast. Eng. 96, 100–117.

Losada, I.J., Maza, M., Lara, J., 2016. A new formulation for vegetation-induced damping under combined waves and currents. Coast. Eng. 107, 1–13.

Luhar, M., Infantes, E., Nepf, H., 2017. Seagrass leaf motion under waves and its impact on wave decay. J. Geophys. Res.: Oceans 122, 3736–3752.

Luhar, M., Nepf, H., 2016. Wave-induced dynamics of flexible leafs. J. Fluids Struct. 61, 20–41.

MACE, 2022. http://www.oceanwave.jp/softwares/mace/index.php?FrontPage. (last Accessed on 30 April 2022).

Mattis, S., Christopher, K., Maya, W., Aggelos, D., Clint, D., 2019. Computational model for wave attenuation by flexible vegetation. J. Waterw. Port Coast. Ocean Eng. 145, 04018033.

Maza, M., Lara, J.L., Losada, I.J., 2013. A coupled model of submerged vegetation under oscillatory flow using Navier–Stokes equations. Coast. Eng. 80, 16–34.

Maza, M., Lara, J.L., Losada, I.J., Ondiviela, B., Trinogga, J., Bouma, T.J., 2015. Large-scale 3-D experiments of wave and current interaction with real vegetation, Part 2: Experimental analysis. Coast. Eng. 106, 73–86.

Mei, C.C., Chan, I.C., Liu, P.L.-F., 2014. Waves of intermediate length through an array of vertical cylinders. Environ. Fluid Mech. 14 (1), 235–261.

Mei, C.C., Chan, I.C., Liu, P.L.-F., Huang, Z., Zhang, W., 2011. Long waves through emergent coastal vegetation. J. Fluid Mech. 687, 461–491.

Mendez, F.J., Losada, I.J., 2004. An empirical model to estimate the propagation of random breaking and nonbreaking waves over vegetation fields. Coast. Eng. 51, 103–118.

Möller, I., Kudella, M., Rupprecht, F., Spencer, T., Paul, M., van Wesenbeeck, B.K., Wolters, G., Jensen, K., Bouma, T.J., Miranda-Lange, M., Schimmels, S., 2014. Wave attenuation over coastal salt marshes under storm surge conditions. Nat. Geosci. 7, 727–731.

Mullarney, J.C., Henderson, S.M., 2010. Wave-forced motion of submerged single-stem vegetation. J. Geophys. Res.: Oceans 115 (C12061).

Narayan, S., Beck, M., W, Wilson, P., Thomas, C.J., Guerrero, A., Shepard, C.C., Reguero, B.G., Franco, G., Ingram, J.C., Trespalacios, D., 2017. The value of coastal wetlands for flood damage reduction in the northeastern USA. Sci. Rep. 7 (9643).

Nardin, W., Edmonds, D., 2014. Optimum vegetation height and density for inorganic sedimentation in deltaic marshes. Nature Geosci. 7, 722–726.

Paul, M., Amos, C.L., 2011. Spatial and seasonal variation in wave attenuation over *Zostera noltii*. J. Geophys. Res. 116, C08019.

Schoutens, K., Heuner, M., Minden, V., Ostermann, T.S., Silinski, A., Belliard, J.-P., Temmerman, S., 2019. How effective are tidal marshes as nature based shoreline protection throughout seasons? Limnol. Oceanogr. 64, 1750–1762.

Sheng, Y.P., Rivera-Nieves, A.A., Zou, R., Paramygin, V.A., 2021. Role of wetlands in reducing structural loss is highly dependent on characteristics of storms and local wetland and structure conditions. Sci. Rep. 11, 5237.

Silinski, A., Heuner, M., Schoelynck, J., Puijalon, S., Schroder, U., Fuchs, E., Troch, P., Bouma, T.J., Meire, P., Temmerman, S., 2015. Effects of wind waves versus ship waves on tidal marsh plants: A flume study on different life stages of *Scirpus maritimus*. PLoS One 10, e0118687.

Stark, T.D., Jafari, N.H., 2015. Ruling on IHNC floodwall failures during Hurricane Katrina. J. Legal Aff. Dispute Resol. Eng. Constr. 7, 06715001.

Sun, F., Carson, R.T., 2020. Coastal wetlands reduce property damage during tropical cyclones. Proc. Natl. Acad. Sci. USA 117, 5719–5725.

van Rijn, L.C., 1993. Principles of Sediment Transport in Rivers, Estuaries and Coastal Seas. Aqua Publications.

van Veelen, T.J., Fairchild, T.P., Reeve, D.E., Karunarathna, H., 2020. Experimental study on vegetation flexibility as control parameter for wave damping and velocity structure. Coast. Eng. 157, 103648.

van Veelen, T.J., Karunarathna, H., Reeve, D.E., 2021. Modelling wave attenuation by quasi-flexible coastal vegetation. Coast. Eng. (164).

Vuik, V., Suh Heo, H.Y., Zhu, Z., Borsje, B.W., Jonkman, S.N., 2018. Stem breakage of salt marsh vegetation under wave forcing: A field and model study. Estuar. Coast. Shelf Sci. 200, 41–58.

Wilson, C.A., Allison, M.A., 2008. An equilibrium profile model for retreating marsh shorelines in southeast Louisiana. Estuar. Coast. Shelf Sci. 80, 483–494.

Wu, W., Ozeren, Y., Wren, D., Chen, Q., Zhang, G., Holland, M., Ding, Y., Kuiry, S.N., Zhang, M., Jadhav, R., Chatagnier, J., Chen, Y., Gordji, L., 2011. SERRI Project: Investigation of Surge and Wave Reduction by Vegetation. Phase I SERRI Report, 80037-01, Oak Ridge National Laboratory.

Zhang, X., Lin, P., Nepf, H., 2021. A simple-wave damping model for flexible marsh plants. Limnol. Oceanogr. 66 (12), 4182–4196.

Zhang, X., Nepf, H., 2021. Wave-induced reconfiguration of and drag on marsh plants. J. Fluids Struct. 100, 103192.

Zhu, L., Chen, Q., 2015. Numerical modeling of surface waves over submerged flexible vegetation. J. Eng. Mech. 141 (A4015001).

Zhu, L., Chen, Q., 2019a. Discussion of field-based numerical model investigation of wave propagation across marshes in the chesapeake bay under storm conditions by Juan L, Garzon, Tyler Miesse and Celso M. Ferreira. Coastal Eng. 149, 1–3.

Zhu, L., Chen, Q., 2019b. Phase-averaged drag force of nonlinear waves over submerged and through emergent vegetation. J. Geophys. Res.: Oceans 124, 4368–4388.

Zhu, Z., Vuik, V., Visser, P.J., Soens, T., van Wesenbeeck, B., van de Koppel, J., Jonkman, S.N., Temmerman, S., Bouma, T.J., 2020a. Historic storms and the hidden value of coastal wetlands for nature-based flood defence. Nat. Sustain. 3, 853–862.

Zhu, L., Zou, Q.P., Huguenard, K., Fredriksson, D.W., 2020b. Mechanisms for the asymmetric motion of submerged aquatic vegetation in waves: A consistent-mass cable model. J. Geophys. Res.: Oceans 125, e2019JC015517.